Research Square

Preprints are preliminary reports that have not undergone peer review.
They should not be considered conclusive, used to inform clinical practice,
or referenced by the media as validated information.

An aerogel Knudsen pump for motionless evaporative cooling of liquid helium below 4 K

Changzhao Pan

pancz@iqasz.cn

Shenzhen International Quantum Academy

Tiantian Xiao

Yu Zhang

Southern University of Science and Technology, Shenzhen International Quantum Academy

Jianqiao Wang

Southern University of Science and Technology, Shenzhen International Quantum Academy

Shu Guo

Shenzhen International Quantum Academy https://orcid.org/0000-0002-2098-8904

Jianbo Tang

Westlake University https://orcid.org/0000-0002-0155-6807

Article

Keywords:

Posted Date: November 25th, 2026

DOI: https://doi.org/10.21203/rs.3.rs-11545171/v1

License: This work is licensed under a Creative Commons Attribution 4.0 International License.
Read Full License

Additional Declarations: There is **NO** Competing Interest.

An aerogel Knudsen pump for motionless evaporative cooling of liquid helium below 4 K

Tiantian Xiao[1,2], Yu Zhang[1,2], Jianqiao Wang[1,2], Shu Guo[2], Jianbo Tang[3], Changzhao Pan[1,2*]

[1]Southern University of Science and Technology, Shenzhen 518055, China

[2]Shenzhen International Quantum Academy, Shenzhen 518048, China

[3]School of Engineering, Westlake University, Hangzhou 310030, China

*pancz@iqasz.cn

Abstract: Cryogenic cooling for quantum technologies often relies on evaporative cooling of liquid helium, but conventional cryostats use mechanical pumps that generate vibrations and electromagnetic noise, compromising measurement precision and qubit coherence. Here we introduce a temperature-gradient-driven, aerogel-based Knudsen pump to achieve motionless evaporative liquid-helium cooling below 4 K. The interconnected nanoporous network and ultralow thermal conductivity of the polyimide aerogel enable a large pressure difference of up to 128.4 kPa under zero-flow conditions and a large helium flow rate of up to 112.9 μmol s^{-1} under near-zero back pressure. The pump's operating pressure up to 1.5 atm, demonstrating thermal-transpiration-driven gas transport above atmospheric pressure, where conventional Knudsen pumping becomes increasingly challenging. The pump cools liquid helium initially at 3.6 K by ~500 mK through sustained evaporation at 30.5 kPa. The present motionless pumping mechanism offers a route to electromagnetically quiet cryogenics for dilution refrigerators and quantum measurement platforms.

Cryogenic refrigeration underpins quantum technologies[1], superconducting technologies[2], and space science[3]. The growing demand for extremely low temperatures, high system-level integration, and long-term non-maintenance operation calls for cryogenic refrigeration technologies that combine precise control with minimal mechanical disturbance. Although alternative cooling concepts based on electrocaloric[4], elastocaloric[5] and magnetocaloric effects[6] have advanced rapidly, liquid-helium evaporative cooling remains an established approach to reaching temperatures below 4 K, which requires continuous vapour removal to reduce the saturation pressure and temperature. Mechanical vacuum pumps can transmit vibrations to cryogenic apparatus, with mechanical disturbances linked to correlated errors in superconducting qubits and electrical noise in spin-qubit measurements[7,8]. Sorption pumps offer low-vibration

operation but require periodic thermal regeneration in single-bed configurations[9,10]. A vibration-free evaporation mechanism that can directly exploit an existing temperature difference would therefore provide an attractive route to low-disturbance pressure control and thermal management in cryogenic systems[11].

The thermal-transpiration effect offers such a possibility. When a temperature gradient is imposed along a micro- or nanoscale pathway, a rarefied gas develops a net mass flow from the cold side towards the hot side, known as the Knudsen effect[12-14]. Because the temperature gradient provides the driving force, Knudsen pumps can use waste heat, solar heating, or the natural temperature difference between a cryogenic stage and its surroundings[15,16]. Knudsen pumps have consequently been explored for microscale vacuum generation[17], fluid transport[18] and gas separation[19,20]. Previous studies have experimentally demonstrated Knudsen pumping down to 77 K[16], while numerical simulations have explored multistage designs incorporating 4 K cold stages[21]. However, operation at liquid-helium temperatures remains experimentally unverified, owing to challenges associated with gas rarefaction, thermal management, and cryogenic structural stability. More importantly, translating Knudsen pumping into evaporative refrigeration requires sustained helium-vapour extraction with sufficient pressure and flow to overcome system resistance and heat loads. Whether these requirements can be met to achieve liquid-helium evaporative cooling remains to be demonstrated experimentally.

The enabling material for cryogenic Knudsen pumping must provide interconnected nanoscale channels for rarefied-gas transport, high porosity for sufficient gas throughput, low thermal conductivity to suppress heat leakage, and mechanical stability under repeated cooling. Porous alumina ceramics used[16] have relatively large pores, low porosity, and high thermal conductivity, which constrain gas transport and increase parasitic heat leakage, limiting their extension to liquid-helium temperatures. Polyimide aerogels offer this combination of an open pore network, thermal insulation and cryogenic mechanical stability[22]. Although thermal-transpiration transport in polyimide aerogels has been demonstrated near room temperature[23,24], their behaviour at deep cryogenic temperatures remains poorly understood. Their potential as the working element of a helium-vapour pump, rather than only as a medium for thermally driven gas transport, had also not been demonstrated.

Here we report a polyimide-aerogel low-temperature Knudsen pump (PIA-LT-KP) that produces strongly enhanced thermal transpiration at cryogenic temperatures, and use it to extract helium vapour without moving components. By integrating multiple

pumping stages with a liquid-helium system, we show that thermal transpiration can sustain helium-vapour extraction and reduce the liquid temperature to 3.13 K. This work reframes a temperature difference, typically a boundary condition or a nuisance heat load, as a direct source of refrigeration. Because dilution refrigerators likewise rely on continuous helium-vapour extraction to sustain ^{3}He circulation[25], this pumping principle could potentially be extended to their gas-circulation systems. Such an approach offers a possible route towards reducing mechanical disturbances in cryogenic refrigeration, particularly for vibration-sensitive quantum measurement platforms.

Building a motionless pump from polyimide aerogel

We built the PIA-LT-KP around a cylindrical polyimide aerogel (PIA), 25.5 mm in diameter and 40 mm long (Fig. 1a), sealed in a thin-walled stainless-steel housing between copper heat exchangers (Fig. 1d). The highly porous nanoscale network of PIA provides transport pathways that favour rarefied-gas flow over a broad range of temperatures and pressures. Its interconnected three-dimensional nanofibrous network features an average pore size of 80-150 nm and a porosity of approximately 90% (Fig. 1a). These numerous nanochannels provide pathways for helium transport, while gas-wall interactions within these channels enable temperature-gradient-driven thermal transpiration.

The low thermal conductivity of PIA is crucial for establishing a large temperature gradient that drives directional gas flow. The thermal conductivity reaches 0.86 mW m^{-1} K^{-1} at 4 K and remains below 20 mW m^{-1} K^{-1} over the temperature range from 4 to 300 K (Fig. 1b). These values are approximately three orders of magnitude lower than those of the conventionally used alumina porous medium[16]. Such ultralow thermal conductivities suppress heat conduction between the hot and cold ends. Consequently, the PIA substantially enhances the temperature gradient and thermal transpiration. Mechanical characterization further shows good cryogenic stability. This stability supports reproducible operation of the PIA-LT-KP under cryogenic conditions. Detailed structural, thermal, and mechanical characterizations of the PIA are provided in the Methods and Supplementary Table 1. Together, these properties of PIA provide a material basis for enhanced thermal transpiration and improved pumping performance at cryogenic temperatures.

The PIA-LT-KP is connected between two closed gas reservoirs in parallel with a valve V_A, forming a sealed gas circuit with a helium leak rate below 10^{-11} Pa m^3 s^{-1} (Fig. 1c). A refrigerator cools the cold end of the PIA-LT-KP, while an electrical heater

supplies heat to the hot end. The pump and the cold head of the refrigerator are housed in a high-vacuum cryostat. The pressures of the two gas reservoirs, P_1 and P_2, are monitored to characterize pressure boost and gas transport. The uncertainty of the complete experimental system is analyzed in Supplementary Note 1. The cooldown performance of the refrigerator and cryogenic assembly is described in Supplementary Note 2.

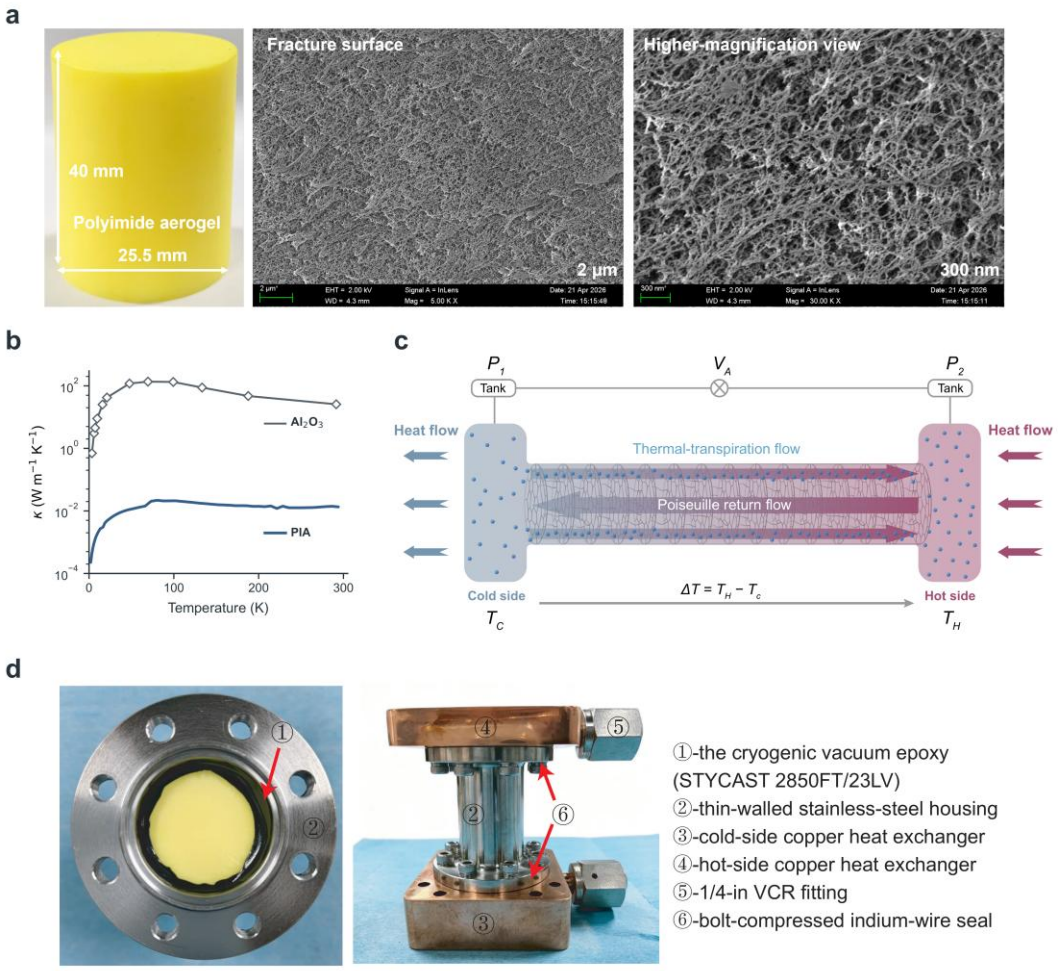

Fig. 1. Material architecture and operating principle of the polyimide-aerogel low-temperature Knudsen pump (PIA-LT-KP). a, Photograph of a cylindrical polyimide aerogel (PIA) specimen (25.5 mm in diameter and 40 mm in height) and scanning electron microscopy images of its fracture surface at two magnifications; scale bars, 2 μm and 300 nm. **b,** Thermal conductivity variation curves of PIA and Al_2O_3 at temperatures ranging from 2 K to 300 K. The PIA data were measured in this work, whereas the Al_2O_3 data were obtained from reference[26]. **c,** Schematic of thermal transpiration through the PIA-LT-KP between reservoirs at cold-side temperature T_C and hot-side temperature T_H ($\Delta T = T_H - T_C$). Thermal-transpiration flow is directed from the cold side towards the hot side, whereas the resulting pressure difference drives an opposing Poiseuille return flow. P_1 and P_2 denote the reservoir pressures and V_A is the inter-reservoir valve. **d,** Photographs

of the PIA mounted in the pump holder and the assembled PIA-LT-KP cell.

Performance evaluation of the PIA-LT-KP

The PIA-LT-KP starts operating when a temperature gradient is established across the PIA. Notably, Knudsen pumping persists deep into the cryogenic regime. With a cold- and hot-end temperature of 3.5 K and 17.6 K, respectively, the PIA-LT-KP generates a pressure difference of approximately 10 kPa (Fig. 2a). With V_A open, the pressure throughout the gas circuit is equalized. Once V_A is closed, pressure falls in the cold-side reservoir and rises in the hot-side reservoir. The initially rapid response slows as the growing pressure difference opposes thermally driven transport, eventually reaching a dynamic equilibrium when thermally driven flow balances the pressure-driven counterflow.

The pressure response exhibits pronounced hysteresis with respect to the externally measured temperature difference (Fig. 2b). During heating, the pressure difference remains negligible below 13 K and then rises to 127 Pa at 34.6 K, whereas during cooling it follows a higher trajectory, reaching 147 Pa at 25 K. This hysteresis is likely associated with the thermal inertia of the PIA, which causes its internal temperature field to lag behind the externally measured temperature difference.

We examine the operating range of PIA-LT-KP over temperatures from 4 to 300 K and initial pressures from 1 to 150 kPa (Fig. 2c). The thermal-transpiration pressure difference is obtained throughout the tested parameter space. The results demonstrate that the PIA-LT-KP can maintain pumping over a broad range of temperatures and pressures. The maximum pressure difference, ΔP_{max}, depends strongly on both the initial pressure and the applied temperature difference. Larger pressure outputs are generally obtained at higher initial pressures and larger temperature differences. At an initial pressure of 66.5 kPa and a temperature difference of 237 K, the four-stage PIA-LT-KP generates a maximum pressure difference of 128.4 kPa. These measurements provide the experimental basis for analyzing the coupled effects of thermal driving and gas rarefaction on pump performance.

To reduce the influence of the applied temperature difference when comparing pressure-boost performance, we define a temperature-normalized pressure difference, K_P,

$$K_P = \frac{\Delta P_{max}}{\Delta T}$$

where K_P represents the maximum pressure difference generated per unit temperature difference.

We use K_P to benchmark the PIA-LT-KP against previously reported porous-media and microfabricated Knudsen pumps (Fig. 2d). At an initial pressure of approximately one atmosphere and a temperature difference of 64 K, the PIA-LT-KP reaches K_P=270 Pa K^{-1}, which is 2.7 times higher than that of the highest value (100 Pa K^{-1}) reported previously for porous-media Knudsen pumps[12].

These results show substantial improvement in pumping performance. More importantly, the PIA-LT-KP maintains measurable pressure generation across a broad range of operating temperatures (including near liquid-helium temperatures) and pressures up to atmospheric pressure. However, generating a maximum pressure difference under zero-flow conditions is distinct from sustaining gas transport against a finite pressure load, and the latter is required for continuous helium-vapour extraction. The measured pressure and flow characteristics therefore provide the experimental basis for translating individual pumping elements into multistage assemblies with application-specific outputs.

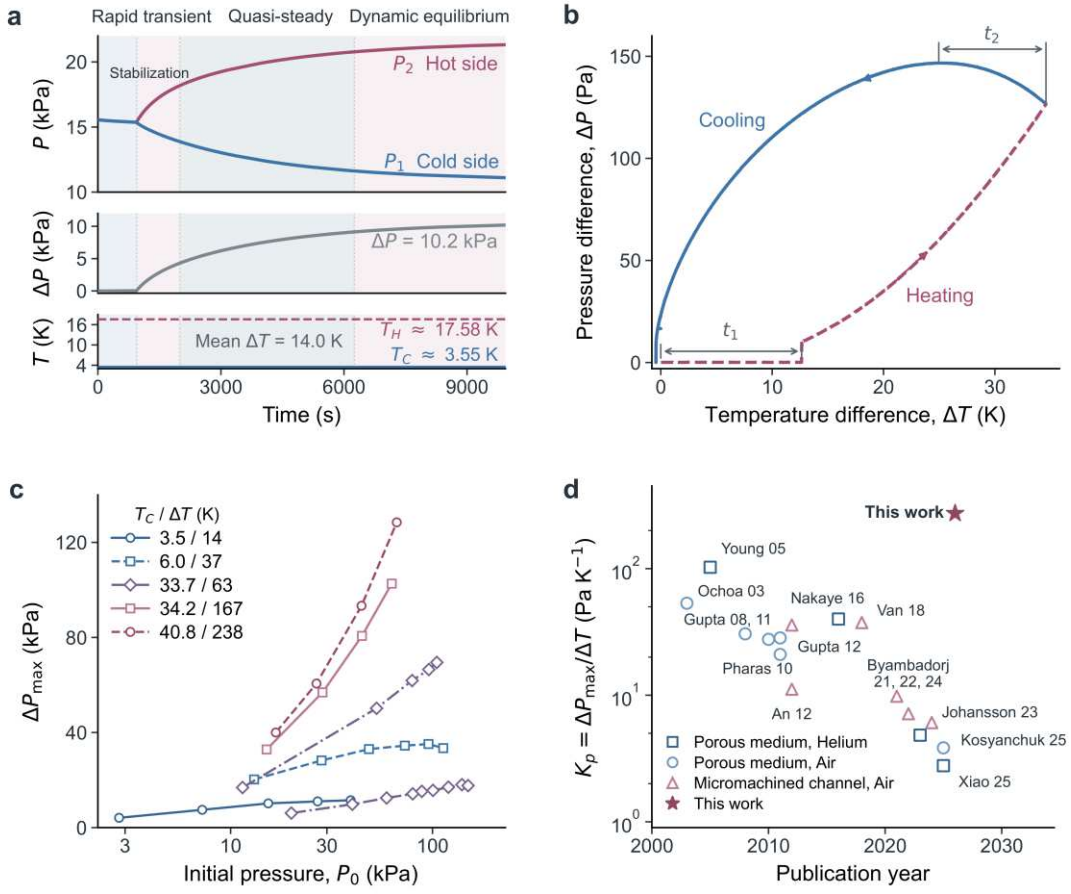

Fig. 2. Demonstration and analysis of the PIA-LT-KP operation. a, Pressure evolution during PIA-LT-KP operation at a filling pressure of 15 kPa, with cold- and hot-end temperatures of 3.5 and 17.6 K, respectively (ΔT = 14.1 K). The pumping process is divided into four distinct stages

(stabilization, rapid transient response, quasi-steady asymptote, dynamic equilibrium) according to the pressure-change rate and internal gas-flow behavior. **b,** Hysteresis loop of the PIA-LT-KP pressure difference as a function of temperature difference. **c,** Experimental results of the PIA-LT-KP developed in this work over a broad operating window spanning 4-300 K and 1-150 kPa. **d,** Comparison of the temperature-normalized pressure difference (K_P) of the PIA-LT-KP developed in this work with values reported in the literatures[16,27-41]. The present work achieves a value of up to 270 Pa K^{-1}, approximately 3 times the highest values reported in the literature considered here.

From pumping performance to multistage design

We next examined how the pressure rise and gas throughput of the PIA-LT-KP could be adjusted, and how individual pumping elements could be combined into an assembly suitable for helium-vapour extraction. The temperature difference across the aerogel provides a direct means of controlling the output. Both the maximum pressure difference and the molar flow rate increase approximately linearly with the temperature difference range examined (Fig. 3a). At an initial pressure of 100 kPa and a temperature difference of 165 K, the maximum pressure difference reaches 33.43 kPa at zero net flow, whereas the maximum molar flow rate reaches 112.87 μmol s^{-1} at zero pressure difference. This corresponds to an area-normalized volumetric flow rate of approximately 167 μL min^{-1} mm^{-2}, exceeding the approximately 8 μL min^{-1} mm^{-2} steady-state flow rate reported for a silica-aerogel Knudsen pump[42]. This trend originates from the stronger thermal driving force across the PIA. Gas rarefaction provides a second governing parameter. Over the experimentally investigated range of Kn = 0.5-4.5, both the maximum pressure difference and the molar flow rate first increase and then decrease with increasing Kn (Supplementary Fig. 3). And temperature-normalized pressure difference (K_P) is generally greater at higher initial pressures and lower mean temperatures within the tested range (Supplementary Fig. 4). Together, these measurements define the conditions under which a single aerogel element delivers useful pumping output.

The output of a single-stage PIA-LT-KP is ultimately limited by the underlying transport mechanism. Multistage configurations provide a route to higher pressure or flow outputs[34,43]. Connecting two PIA-LT-KPs in series increases the pressure difference from 11.71 kPa for a single stage to 17.66 kPa, corresponding to a factor of 1.5 (Fig. 3b). The molar flow rate decreases in this configuration. By contrast, a two-stage parallel configuration increases the molar flow rate from 33.08 to 50.64 μmol s^{-1}, corresponding to a factor of 1.53. The pressure difference also increases slightly (from

11.71 kPa to 12.47 kPa). These results show that a series connection favours pressure boost, whereas a parallel connection favours gas throughput. The gains are smaller than a simple linear addition of the individual pump outputs because additional stages introduce interstage flow resistance and associated pressure losses.

To determine how many elements are needed for a prescribed pressure rise, we develop a multistage model using the measured flow-pressure characteristics of an individual PIA-LT-KP and conservation of gas in the connected volumes (Fig. 3c). We first characterized the flow-pressure relationship of one element at a fixed temperature difference and different initial pressures, establishing the pressure- and flow-dependent inputs to the model (Supplementary Note 3). Then mass conservation is applied to every gas volume, and the pressures and stage-wise flows are updated iteratively to predict the response of the complete assembly. The governing relationships, boundary conditions, and numerical procedure are detailed in Supplementary Note 4. We validated the model against a two-stage pump at several initial pressures (Fig. 3d). The calculated pressure build-up follows the measured response, with deviations in the steady maximum pressure difference remaining below 5% (Supplementary Table 3). Furthermore, the predicted maximum molar flow rates agree with measurements to within 10%. These comparisons demonstrate that the model can reliably predict both pressure boost and gas transport in multistage PIA-LT-KPs over the investigated pressure range.

Reversing the calculation yields a design map that links the initial pressure and the required pressure rise to the number of stages (Fig. 3e). The design map therefore provides a quantitative basis for coordinating the stage number, operating pressure, and required pressure rise. Experimental conditions fall within the predicted regions (Fig. 3e), validating the inverse-design framework. The model thus provides a direct route from pressure requirement to stage number. These results establish a quantitative route from the performance of individual aerogel elements to the design of multistage PIA-LT-KPs with a prescribed pressure output, providing a basis for their integration into practical cryogenic systems.

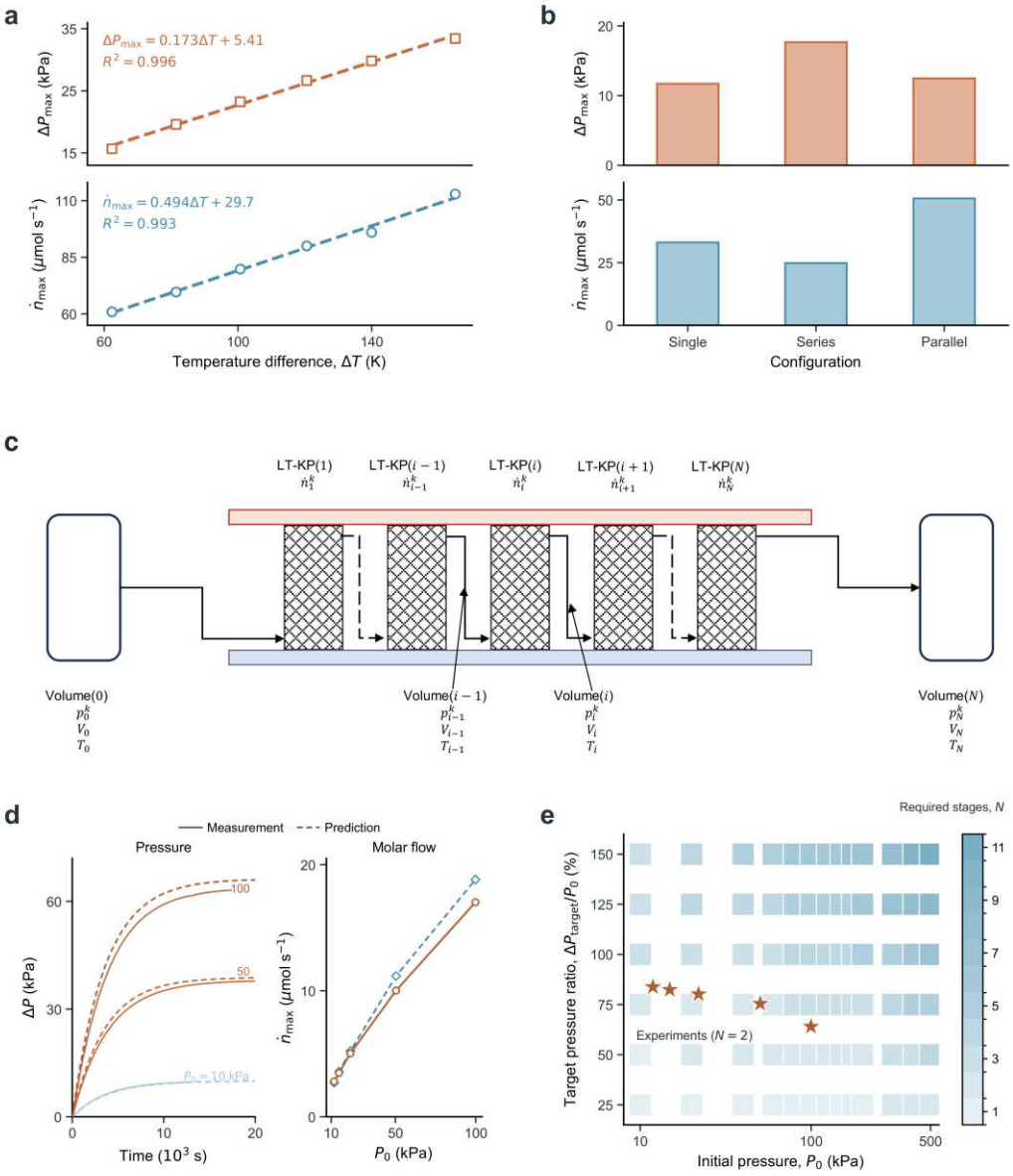

Fig. 3. Performance scaling and predictive design of multistage PIA-LT-KPs. a, Effect of the temperature difference on PIA-LT-KP pressure-boosting performance and gas transport capability ($P_0 = 100$ kPa). **b,** Comparison of pumping performance between series and parallel configurations ($P_0 = 60$ kPa, $\Delta T = 60$ K). **c,** Performance prediction model for the N-stage PIA-LT-KP, showing the pressure, volume, temperature and molar flow rate at different locations. Subscripts denote spatial positions and superscripts denote time steps. **d,** Comparison between predicted and measured pressure and flow performance. **e,** Predictive design map for determining the required stage number of PIA-LT-KP for a given initial pressure and target pressure difference, with experimental operating points indicated.

Cryogenic Knudsen pumping drives liquid-helium evaporation cooling

We further asked whether the pressure and flow generated by the motionless PIA-LT-KP could be translated into a more demanding function: cooling liquid helium by continuously extracting its vapour. We therefore developed a liquid-helium evaporative refrigeration system incorporating a four-stage PIA-LT-KP. The experimental implementation, including the Gifford-McMahon cryocooler, cold trap, condenser, liquid-helium pot, and PIA-LT-KP, is shown in Fig. 4a, and the corresponding refrigeration pathway is illustrated schematically in Fig. 4b. High-purity helium was precooled at the first stage of the refrigerator, condensed near 4 K at the second stage, further cooled in a counterflow heat exchanger, and finally expanded through a throttling valve into a liquid-helium pot. Evaporative cooling was achieved by reducing the vapour pressure above the liquid helium. We first validated the refrigeration pathway using a conventional dry vacuum pump (Supplementary Note 5).

After this baseline validation, the mechanical pump was replaced by the four-stage PIA-LT-KP integrated into the cryogenic system (Fig. 4a). In this configuration, helium vapour was withdrawn from the liquid-helium pot at P_2 through the PIA-LT-KP towards P_3, with the resulting pressure reduction driving continued evaporation (Fig. 4b). Before activation, the liquid-helium pot stabilized at 55 kPa and 3.61 K (Fig. 4c, stage I). This initial equilibrium period lasted for approximately 2 min and showed no measurable cooling. After activation of the PIA-LT-KP, its outlet pressure (P_3) first increased, while the pressure and temperature of the liquid-helium pot remained unchanged. This delay lasted for approximately 3 min (Fig. 4c, stage II-1). Cooling started in stage II-2, during which the pot pressure (P_2) and temperature decreased simultaneously (Fig. 4c). This response indicates that the PIA-LT-KP removes helium vapour from the gas space above the liquid and reduces the pressure. The system then entered a sustained evaporative-cooling regime (Fig. 4c, stage III). As the pot pressure decreased further, the corresponding saturation temperature of liquid helium also decreased. Part of the liquid therefore evaporated to restore liquid-vapour equilibrium. This evaporation absorbed latent heat, continuously reducing the pot temperature. Both the pressure and temperature decreased monotonically over an extended period. This behaviour shows that the PIA-LT-KP can maintain continuous helium-vapour extraction and a net cooling effect.

At longer times, the system approached a quasi-steady regime (Fig. 4c, stage IV), and the rates of pressure and temperature decrease gradually diminished. After 27 h, the pressure fell to 30.5 kPa and the temperature to 3.13 K, corresponding to reductions of

24.5 kPa and 0.48 K, respectively. The liquid-helium pot cooled from 3.61 to 3.13 K over 27 h, corresponding to a baseline net cooling power of approximately 0.505 μW. This value quantifies the cooling retained by the system and thus provides a conservative measure of the evaporative cooling generated by the PIA-LT-KP, because parasitic heat loads are not included. The coupled pressure reduction and sustained temperature decrease demonstrate that multistage Knudsen pumping can directly drive depressurization-induced evaporation cooling of liquid helium. The measured pressure-temperature trajectory remained within 0.05 K of the helium saturation relation (Supplementary Fig. 9), providing thermodynamic evidence that the cooling resulted from pressure-induced evaporation. The relatively slow cooling reflects the limited helium-vapour throughput of the PIA-LT-KP and the parasitic heat loads of the experimental system. Nevertheless, this experiment demonstrates the feasibility of liquid-helium evaporative cooling through thermal-transpiration-driven vapour extraction without mechanical pumping.

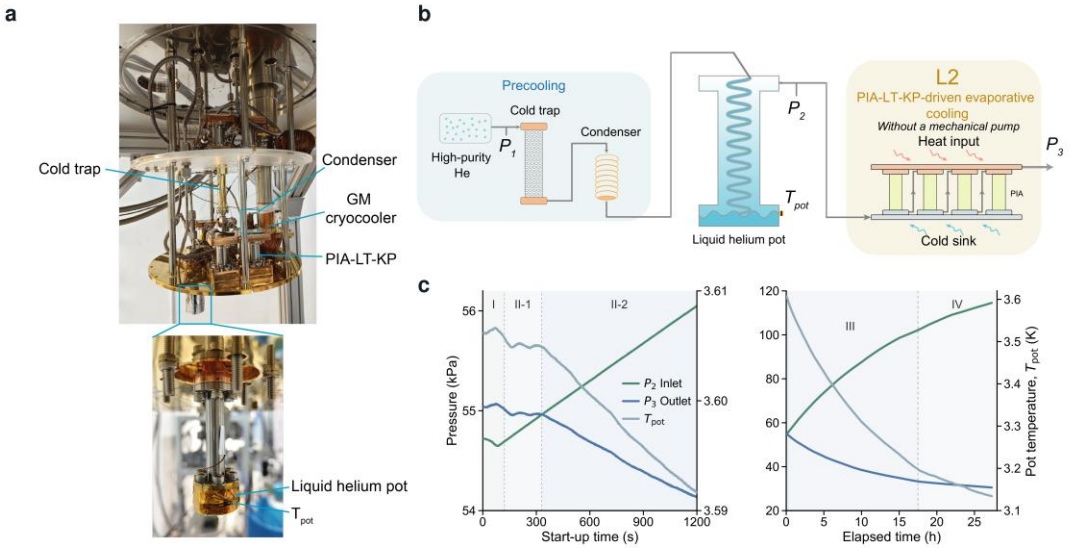

Fig. 4. Liquid-helium evaporative cooling driven by the PIA-LT-KP. a, Photograph of the open helium liquefaction and evaporative-cooling system, showing the cold trap, condenser, Gifford-McMahon (GM) cryocooler, PIA-LT-KP and liquid-helium pot. The enlarged view shows the liquid-helium pot and the location of the temperature measurement (T_{pot}). **b,** Schematic of the experimental process. High-purity helium at P_1 is precooled and liquefied before accumulating in the liquid-helium pot at P_2. The 4-stage PIA-LT-KP subsequently drives helium-vapour extraction towards P_3, promoting liquid-helium evaporation and cooling without a mechanically driven pump. **c,** Complete evolution of the PIA-LT-KP inlet pressure (P_2) and outlet pressure (P_3) and the pot temperature during the process. Stage I represents the steady state before PIA-LT-KP start-up,

whereas Stage II corresponds to the transient response following PIA-LT-KP start-up. During Stage III, the PIA-LT-KP operated continuously for 17 h, resulting in sustained depressurization and cooling. The system subsequently entered a quasi-steady state that persisted for approximately 10 h (Stage IV).

Conclusions and outlook

We developed a polyimide-aerogel low-temperature Knudsen pump (PIA-LT-KP) and evaluated its operation over 4-300 K and initial pressures of 1-150 kPa. The pump generates a maximum pressure difference of 128.4 kPa and a maximum molar flow rate of 112.9 μmol s^{-1}, with a temperature-normalized pressure difference of up to 270 Pa K^{-1}. Parameter mapping further identifies how thermal driving force, gas rarefaction, and pump configuration govern pressure and flow outputs. We also developed a predictive model for multistage PIA-LT-KPs that enables inverse design by directly determining the minimum number of stages required to achieve a prescribed pressure rise.

We further integrated a multistage PIA-LT-KP into a liquid-helium system to demonstrate thermal-transpiration-driven evaporative cooling. Continuous helium-vapour extraction reduced the pot pressure from 55.0 to 30.5 kPa, and the temperature from 3.61 to 3.13 K, and the pressure-temperature trajectory remained close to the saturated vapour-pressure relation. This experiment demonstrates that a temperature difference across a porous medium can be converted directly into gas flow, pressure, and refrigeration without mechanical pumping.

Future improvements should focus on increasing effective flow area and optimizing pore structure, while reducing interstage resistance and parasitic heat leakage. Extending the approach to other gases, temperatures, and pressures will also be important. More broadly, thermal-transpiration-driven pumping provides a motionless platform for cryogenic gas transport, pressure regulation, and refrigeration, with potential applications where vibration, reliability and maintenance are critical. These include evaporative refrigeration, cryogenic fluid management, and gas compression, as well as gas handling in hydrogen-energy, space and other extreme-environment systems.

Methods

Structural characterization of polyimide aerogels

Polyimide aerogels (PIA, KLG9-SH-B01) are obtained commercially from IBIH in

Cangzhou, Hebei, China. The morphology and pore structure of the polyimide aerogels were characterized using scanning electron microscopy (SEM). Samples were cut from the interior of the aerogel monoliths to expose representative cross-sections and were attached to aluminum foil using conductive adhesive, followed by gold sputter coating on the surface. SEM analysis was performed on a ZEISS Gemini SEM 500 instrument equipped with an InLens detector, at an accelerating voltage of 2.00 kV and a working distance of 4.3 mm. Images were acquired at multiple magnifications to examine the overall porous architecture and local pore morphology. The specific surface area and pore size distribution of PIA were analyzed using a specific surface area and pore size analyzer (JW-BK222). Nitrogen adsorption and desorption isotherms were obtained at 77.35 K. The specific surface area of PIA was calculated by the Brunauer-Emmett-Teller (BET) method.

Low-temperature thermal conductivity evaluation

The thermal conductivity of PIA over the full temperature range of 2 K-300 K was evaluated using a fully cryogen-free Physical Property Measurement System, PPMS® DynaCool™ manufactured by Quantum Design. The system provides a temperature range of 1.9 K-400 K and a high-vacuum environment better than 10^{-4} Torr. Thermal conductivity measurements of PIA were performed using the Thermal Transport Option (TTO) in continuous mode. The measurement is based on the steady-state axial heat-flow method. According to the one-dimensional Fourier law of heat conduction, $Q = \kappa A \Delta T / L$, the thermal conductivity of PIA at different temperatures was calculated from the recorded sample dimensions, temperature difference between the measurement points, and applied heating power.

Low-temperature mechanical properties evaluation

The evaluation was carried out using the facilities of the Cryogenic Mechanics Laboratory at the Technical Institute of Physics and Chemistry, Chinese Academy of Sciences. The compressive properties, tensile properties, and Poisson's ratio of PIA were measured at liquid-helium temperatures. In addition, its coefficient of thermal expansion was evaluated at liquid-nitrogen temperatures. The specimen requirements, testing equipment, test conditions, experimental procedures, and data processing methods were implemented in accordance with the relevant provisions of GJB 1585A-2004. The detailed test results are summarized in Supplementary Table 1.

Evaluation of the permeability

The flow capability of fluids within the internal pores of PIA is described by its permeability, which is defined according to Darcy's law.

$$K_D = \frac{\mu L Q_m}{A \Delta P}$$

As indicated by the equation, the permeability is proportional to the geometrical height (L) of PIA, the viscosity (μ) of the fluid, and the gas flow rate (Q_m), while it is inversely proportional to the pressure difference across the two sides (ΔP)and the cross-sectional area (A). Helium was selected as the test fluid. During the experiment, the pressures on both sides of PIA, P1 and P2, as well as the flow rate Q, were recorded. The Q-ΔP relationship curve was obtained through multi-point measurements. The device used for permeability measurement and the results are provided in Supplementary Fig. 2.

Fabrication of the PIA-LT-KP

The cylindrical PIA element was bonded and sealed peripherally to a thin-walled stainless-steel tube using a low-temperature vacuum-grade epoxy (STYCAST 2850FT/23LV). Both ends were connected to copper heat exchangers with internal cavities, sealed with indium wire and secured with bolts to form a single-stage PLA-LT-KP. VCR fittings on the sides of the copper heat exchangers enabled subsequent interstage connections. A cross-sectional schematic of the PLA-LT-KP is provided in the Supplementary Fig. 10.

Cryogenic PIA-LT-KP experimental platform

A cryogenic experimental platform was constructed to characterize the pressure and flow performance of the PIA-LT-KP over a wide temperature and pressure range. The platform consists of five parts: the key PIA-LT-KP, a two-stage Gifford-McMahon cryocooler (Sumitomo, RDK-415D2, 1.5 W @ 4.2 K), a vacuum system, a gas circuit system, and a data acquisition and control system. The vacuum chamber was evacuated to below 10^{-5} Pa before cooling to minimize convective heat transfer and prevent gas condensation on the cryogenic components.

The cold ends of the PIA-LT-KPs were thermally anchored to the first and second cold stages of the G-M cryocooler via oxygen-free copper adapter plates, with four pumps mounted on each plate. At each stage, the hot ends of the four pumps were thermally coupled to a common oxygen-free copper hot plate equipped with a resistive heater (MP930-20.0%-1%) to control temperature. The cold- and hot-end temperatures, T_C and T_H, respectively, were determined using temperature sensors bonded to the

corresponding oxygen-free copper plates. Cernox sensors (measurement range: 1.3-360 K, accuracy: 5 mK) were used below 50 K, whereas platinum resistance thermometers (measurement range: -200℃~600℃, accuracy: IEC60751 class A) were used above 50 K. The temperature difference across the pumping medium was defined as $\Delta T = T_H - T_C$.

The two sides of PIA-LT-KP were connected to sealed gas reservoirs, forming a closed gas circuit. Before each experiment, the gas circuit was subjected to several evacuation-helium refill cycles to minimize residual gas impurities. It was subsequently charged with high-purity helium to the prescribed initial pressure. Absolute pressures on the cold and hot sides, P1 and P2, respectively, were measured using two absolute pressure sensors (JYB-D3152-BD, measurement range: 0-150 kPa, accuracy: $\pm$0.1%FS). The pressure difference across the PIA-LT-KP, ΔP, was independently monitored using a differential pressure transducer (JYB-D3151-BD, measurement range: 0-50 kPa, accuracy: $\pm$0.075%FS). Temperature signals were acquired using a Kelvinion Monitor (MultiFields), which supports measurements down to 300 mK with a temperature resolution of 1 mK. Pressure signals were acquired using an NI 9203 module (National Instruments). The Supplementary provides detailed analyses of the measurement uncertainties of the experimental system, as well as an experimental assessment of its overall cooling performance.

Pressure-boosting measurements

The maximum pressure difference of the PIA-LT-KP was measured under zero-flow conditions. At the beginning of each experiment, the valve (V_A) was kept open, and the gas circuit was charged with helium. As the cold end of the PIA-LT-KP was cooled, the pressure in the gas circuit decreased. The prescribed temperature difference was then established and maintained until $\left|\frac{d\Delta T}{dt}\right| < 0.02$ K/min over a 5-min interval. With V_A open, the system was allowed to equilibrate until P1 and P2 became indistinguishable within the measurement resolution. The mean pressure was also required to show no appreciable systematic drift over a 5-minute interval. The pressure averaged over this interval was taken as the initial pressure, P_0.

The valve was then closed to isolate the two sides of the PIA-LT-KP. The imposed temperature difference drove helium from the cold side to the hot side. As a result, a pressure difference gradually developed across the PIA-LT-KP. The temporal evolutions of $P_1(t)$, $P_2(t)$, and $\Delta P(t)$ were recorded. The system was considered to

have reached a quasi-steady state when $\left|\frac{d\Delta P}{dt}\right| < 2\ \mathrm{Pa/min}$ over a 5-min interval. Under this condition, the net gas flow rate approached zero. The mean pressure difference over this interval was recorded as the maximum zero-flow pressure difference (ΔP_{max}) of the PIA-LT-KP.

Calculation of the molar flow rate

The maximum molar flow rate of the PIA-LT-KP was determined under zero-pressure-difference conditions. The prescribed temperature difference was first established with the valve (V_A) open. Under this condition, the two sides of the PIA-LT-KP remained connected and there was no pressure difference in the gas circuit ($\Delta P = 0$). Valve V_A was then closed, and this moment was defined as t=0. At t=0, the pressure difference remained zero and the molar flow rate was therefore at its maximum. According to the ideal gas law, the instantaneous molar flow rate was calculated as:

$$\dot{n} = \frac{V}{2RT}\frac{d\Delta P(t)}{dt}$$

where V is the volume of the gas reservoir, R is the universal gas constant, R=8.314 J mol^{-1} K^{-1}, and T is the ambient temperature. The term $\frac{d\Delta P(t)}{dt}$ represents the temporal rate of change of the pressure difference. The initial slope of the $\Delta P(t)$ curve was used to determine the molar flow rate at t=0. This value was taken as the maximum molar flow rate of the PIA-LT-KP, $\dot{n}_{max}$.

Wide-temperature and wide-pressure measurements

The operating envelope of the PIA-LT-KP was characterized by systematically varying the temperature from 4 to 300 K and the initial pressure from 1 to 100 kPa. The experimental temperature was varied by adjusting the heating power supplied to the hot end of the PIA-LT-KP. The gas circuit was externally connected to a high-purity helium cylinder and a vacuum pump to regulate the system pressure. Following the procedure described above, ΔP_{max} and $\dot{n}_{max}$ were determined for each temperature-pressure operating condition.

Performance prediction of multistage PIA-LT-KP

The prediction is based on the pressure difference-flow rate characteristics of the PIA-LT-KP and the conservation of mass. The maximum pressure difference, ΔP_{max}, and maximum molar flow rate, $\dot{n}_{max}$, depend on the operating temperature and initial pressure. The relationship between the molar flow rate and pressure difference is given

by:

$$\frac{\dot{n}(T,\bar{P},\Delta P)}{\dot{n}_{max}(T,\bar{P})} = 1 - \frac{\Delta P}{\Delta P_{max}(T,\bar{P})}$$

During each time step, the molar flow rate through each pump (i) was calculated from the following mass-conservation relationship:

$$n_i^{k+1} = n_i^k + \frac{dn_i^k}{dt} \times \Delta t$$

The pressure at the next time step was then calculated as:

$$P_i^{k+1} = P_i^k + \Delta t \times \frac{RT_i}{V_i} \times (\dot{n}_i^k - \dot{n}_{i+1}^k)$$

The calculation was iterated in MATLAB to obtain the pressure evolution at each location in the multistage PIA-LT-KP. The pressure difference across the multistage PIA-LT-KP was subsequently determined as a function of time. The pressure difference-flow rate characteristics of a single-stage PIA-LT-KP, the boundary conditions, and the detailed derivation of the model are provided in the Supplementary.

Stage-number design method

An inverse design procedure was developed to determine the minimum number of PIA-LT-KP stages required to achieve a prescribed pressure difference. The procedure was based on the steady-state pressure characteristics of the multistage system. The two ends of the multistage PIA-LT-KP are closed, and the molar flow rate approaches zero at steady state. The pressure difference generated by each stage satisfies:

$$\Delta P_i = P_i - P_{i-1} = \Delta P_{max}(\bar{P}_i)$$

where $\bar{P} = (P_i + P_{i-1})/2$.

The steady-state pressure distribution was further constrained by conservation of the total number of moles in the closed gas circuit:

$$\sum_{i=0}^{N} \frac{P_i V_i}{RT_i} = \sum_{i=0}^{N} \frac{P_{init} V_i}{RT_i}$$

The coupled nonlinear equations were solved to obtain the steady-state pressures $P_0, \ldots\ldots, P_N$. The maximum overall pressure difference generated by an N-stage PIA-LT-KP is calculated as:

$$\Delta P_{ss}(N, P_{init}) = P_N - P_0$$

For a prescribed initial pressure P_{init} and target pressure difference ΔP_{target}, the minimum required number of stages was determined according to:

$$N_{req} = min\{N \in \mathrm{N}^+ : \Delta P_{ss}(N, P_{init}) \geq \Delta P_{target}\}$$

This procedure converts the forward prediction of multistage pressure generation into an inverse design framework. It directly determines the minimum number of stages required to achieve a specified target pressure difference.

Helium evaporation-cooling experiments

The multistage PIA-LT-KP was integrated into an open helium liquefaction system. The outlet of the liquid-helium pot was connected to the low-pressure side of a 4-stage PIA-LT-KP, and the pump outlet was connected to a helium-recovery reservoir. All connections were helium-leak tested before operation. The liquid-helium pot pressure and PIA-LT-KP outlet pressure were measured using two absolute pressure sensors (JYB-D3152-BD, measurement range: 0-150 kPa, accuracy: $\pm$0.1%FS). Liquid-helium-pot temperature was measured using a Cernox sensor (measurement range: 1.3-360 K, accuracy: 5 mK).

Data availability

The data that support the findings of this study are available within the article and its Supplementary Information. Source data are provided with this paper.

References

1 Xue, X. *et al.* CMOS-based cryogenic control of silicon quantum circuits. *Nature* **593**, 205-210 (2021).
2 MacManus-Driscoll, J. L. & Wimbush, S. C. Processing and application of high-temperature superconducting coated conductors. *Nat. Rev. Mater.* **6**, 587-604 (2021).
3 Han, Y. & Zhang, A. Cryogenic technology for infrared detection in space. *Sci. Rep.* **12**, 2349 (2022).
4 Han, D. *et al.* Self-oscillating polymeric refrigerator with high energy efficiency. *Nature* **629**, 1041-1046 (2024).
5 Zhou, G. *et al.* Achieving kilowatt-scale elastocaloric cooling by a multi-cell architecture. *Nature* **639**, 87-92 (2025).
6 Hou, H., Qian, S. & Takeuchi, I. Materials, physics and systems for multicaloric cooling. *Nat. Rev. Mater.* **7**, 633-652 (2022).
7 Kono, S. *et al.* Mechanically induced correlated errors on superconducting qubits with relaxation times exceeding 0.4 ms. *Nat. Commun.* **15** (2024).
8 Kalra, R. *et al.* Vibration-induced electrical noise in a cryogen-free dilution refrigerator: Characterization, mitigation, and impact on qubit coherence. *Review of Scientific Instruments* **87** (2016).
9 Sam, A. A., Dutta, R., Abraham, D., Ghosh, P. & Pesyridis, A. A review on design, operation and applications of cold-compressors in large-scale helium liquefier/refrigerator systems. *Cryogenics* **132**, 103700 (2023).

10 Cao, H., Liu, B. & Qin, L. Sorption cryogenic cooling: Fundamentals, progress, and outlook. *Appl. Therm. Eng.* **213**, 118680 (2022).
11 Straub, A. P., Yip, N. Y., Lin, S., Lee, J. & Elimelech, M. Harvesting low-grade heat energy using thermo-osmotic vapour transport through nanoporous membranes. *Nat. Energy* **1**, 16090 (2016).
12 Wang, X. W., Su, T., Zhang, W. Q., Zhang, Z. & Zhang, S. Knudsen pumps: a review. *Microsyst. Nanoeng.* **6**, 26 (2020).
13 Reynolds, O. The Dimensional Properties of Matter in the Gaseous State. *Nature* **19**, 435-437 (1879).
14 Knudsen, M. Molecular Effusion and Transpiration. *Nature* **80**, 491-492 (1909).
15 Kugimoto, K., Hirota, Y. & Kizaki, Y. Motionless heat pump – A new application of thermal transpiration. *AIP Conf. Proc.* **1786**, 080004 (2016).
16 Xiao, T. T. *et al.* First implementation of a novel low-temperature-driven motionless pump. *Phys. Fluids* **37**, 102007 (2025).
17 McNamara, S. & Gianchandani, Y. B. On-chip vacuum generated by a micromachined Knudsen pump. *J. Microelectromech. Syst.* **14**, 741-746 (2005).
18 Kugimoto, K., Hirota, Y., Yamauchi, T., Yamaguchi, H. & Niimi, T. Design and demonstration of Knudsen heat pump without moving parts free from electricity. *Appl. Energy* **250**, 1260-1269 (2019).
19 Qin, Y. & Gianchandani, Y. B. A fully electronic microfabricated gas chromatograph with complementary capacitive detectors for indoor pollutants. *Microsyst. Nanoeng.* **2**, 15049 (2016).
20 Zhao, X. *et al.* Monolithic integration of Knudsen pumps to form a complete, self-sufficient fluidic system for microscale gas chromatography. *Microsyst. Nanoeng.* **11**, 242 (2025).
21 Xiao, T. T., Liao, Y., Liu, X. M. & Pan, C. Numerical investigation of the performance and gas flow characteristics of a novel low-temperature-driven multistage Knudsen pump. *Cryogenics* **152**, 104215 (2025).
22 Cheng, Y. *et al.* Super-elasticity at 4 K of covalently crosslinked polyimide aerogels with negative Poisson's ratio. *Nat. Commun.* **12**, 4092 (2021).
23 Zhao, Y.-B. *et al.* An aerogel-based light-driven knudsen pump approaching complete passive capturing of airborne particles in wide size ranges. *Fundam. Res.* (2025).
24 Zhao, S. *et al.* Dimensional and Structural Control of Silica Aerogel Membranes for Miniaturized Motionless Gas Pumps. *ACS Appl. Mater. Interfaces* **7**, 18803-18814 (2015).
25 Zu, H., Dai, W. & de Waele, A. T. A. M. Development of dilution refrigerators—A review. *Cryogenics* **121** (2022).
26 Uhlig, K. Alumina shunt for precooling a cryogen-free 4He or 3He refrigerator. *Cryogenics* **79**, 35-37 (2016).
27 Ochoa, F., Eastwood, C., Ronney, P. D. & Dunn, B. Thermal transpiration based microscale propulsion and power generation devices. in *Seventh International Workshop on Microgravity Combustion and Chemically Reacting Systems.* (NASA Glenn Research Center).

28 Young, M., Han, Y. L., Muntz, E. P. & Shiflett, G. Characterization and Optimization of a Radiantly Driven Multi-Stage Knudsen Compressor. *AIP Conf. Proc.* **762**, 174-179 (2005).
29 Gupta, N. K. & Gianchandani, Y. B. Thermal transpiration in zeolites: A mechanism for motionless gas pumps. *Appl. Phys. Lett.* **93**, 193511 (2008).
30 Gupta, N. K. & Gianchandani, Y. B. Porous ceramics for multistage Knudsen micropumps-modeling approach and experimental evaluation. *J. Micromech. Microeng.* **21**, 095029 (2011).
31 Gupta, N. K. & Gianchandani, Y. B. Thermal transpiration in mixed cellulose ester membranes: Enabling miniature, motionless gas pumps. *Microporous Mesoporous Mater.* **142**, 535-541 (2011).
32 Pharas, K. & McNamara, S. Knudsen pump driven by a thermoelectric material. *J. Micromech. Microeng.* **20**, 125032 (2010).
33 Gupta, N. K., An, S. & Gianchandani, Y. B. A Si-micromachined 48-stage Knudsen pump for on-chip vacuum. *J. Micromech. Microeng.* **22**, 105026 (2012).
34 An, S., Gupta, N. K. & Gianchandani, Y. B. A Si-Micromachined 162-Stage Two-Part Knudsen Pump for On-Chip Vacuum. *J. Microelectromech. Syst.* **23**, 406-416 (2014).
35 Nakaye, S. & Sugimoto, H. Demonstration of a gas separator composed of Knudsen pumps. *Vacuum* **125**, 154-164 (2016).
36 Van Toan, N., Inomata, N., Trung, N. H. & Ono, T. Knudsen pump produced via silicon deep RIE, thermal oxidation, and anodic bonding processes for on-chip vacuum pumping. *J. Micromech. Microeng.* **28**, 055001 (2018).
37 Byambadorj, T., Qin, Y. & Gianchandani, Y. B. Blocking Pressure Enhancement in SOI Through-Wafer Monolithic Knudsen PUMPs. in *2022 IEEE 35th International Conference on Micro Electro Mechanical Systems (MEMS).* 43-46.
38 Byambadorj, T., Zhao, X., Qin, Y. & Gianchandani, Y. B. Monolithic SOI through-wafer Knudsen pumps with mechanically robust Si channels. *Sens. Actuators A Phys.* **365**, 114825 (2024).
39 Johansson, M. V. *et al.* Temperature gradient effects on gas flow through microporous media. *Exp. Therm. Fluid Sci.* **148**, 110983 (2023).
40 Kosyanchuk, V., Petrov, A., Kik, M., Yagodina, M. & Seredenko, R. Theoretical and experimental study of 3D-printed Knudsen pump with liquid cooling. *Int. J. Heat Mass Transf.* **249**, 127178 (2025).
41 Byambadorj, T., Cheng, Q., Qin, Y. & Gianchandani, Y. B. A monolithic Si-micromachined four-stage Knudsen pump for μGC applications. *J. Micromech. Microeng.* **31**, 034001 (2021).
42 Zhao, S. *et al.* Additive manufacturing of silica aerogels. *Nature* **584**, 387-392 (2020).
43 An, S., Qin, Y. & Gianchandani, Y. B. A Monolithic High-Flow Knudsen Pump Using Vertical Al2O3 Channels in SOI. *J. Microelectromech. Syst.* **24**, 1606-1615 (2015).

Acknowledgements

This work was supported by the Guangdong Pearl River Talent Plan (2023QN10X795). We thank Shuai Ma and Xiaolin Xie for their assistance with the preparation of engineering drawings and mechanical fabrication; Liming Han for support with the implementation of the data acquisition and control system; and Kuifan Zha for assistance with the integration, commissioning, and troubleshooting of the overall experimental system.

Author contributions

T.X. and C.P. conceived the research concept. T.X. designed and constructed the experimental setup, designed the pump components, conducted the experiments and wrote the original draft of the manuscript. Y.Z. revised the manuscript and completed the data visualization. J.W. and S.G. performed the thermal conductivity measurements of the polyimide aerogel. S.G., J.T. and C.P. reviewed and edited the manuscript. All authors discussed the results and approved the final manuscript.

Competing interests

The authors declare no competing interests.

Supplementary Files

This is a list of supplementary files associated with this preprint. Click to download.

- NMEsupplementary.docx